Continuum Mech. Thermodyn.
https://doi.org/10.1007/s00161-020-00924-x

ORIGINAL ARTICLE

Dan-Andrei Şerban · Radu Negru · Hannelore Filipescu · Liviu Marşavina

Investigations on the influence of the triaxial state of stress on the failure of polyurethane rigid foams

Received: 24 March 2020 / Accepted: 28 August 2020

Abstract This paper investigates the failure strain as a dependence of the stress triaxiality and the Lode angle parameter for polyurethane rigid foams (PUR) of two densities (100 and 300 kg/m^3). Tests were carried out in tension for various configurations, resulting in different states of stress triaxiality at various Lode angles in the critical areas. The failure strain was determined for each setup using finite element analysis, as the tests were replicated with numerical models. The displacement at failure recorded in the experiments was imposed for the models, determining the failure strain as a function of stress triaxiality and the Lode angle parameter. The results were validated through the analysis of the failure of sandwich structures with aluminium faces and PUR cores.

Keywords PUR foam · Failure · Stress triaxiality · Experiment · Numerical simulation

List of symbols

d	Plastic displacement
D	Damage evolution parameter
e^{c}	Logarithmic compressive strain
e^{t}	Logarithmic tensile strain
I_1	First invariant of the stress tensor
J_2	Second invariant of the deviatoric stress tensor
J_3	Third invariant of the deviatoric stress tensor
p	Hydrostatic pressure
p^{c}	Yield stress in hydrostatic compression
p^{t}	Yield stress in hydrostatic tension
q	von Mises equivalent stress
r	Normalized third invariant
s^{c}	True compressive stress
s^{t}	True tensile stress
γ	Bai–Wierzbicki Lode angle-dependent parameter
ε^{c}	Engineering compressive strain

Communicated by Luca Placidi and Emilio Barchiesi.

D.-A. Şerban (✉)· R. Negru · L. Marşavina
Department of Mechanics and Strength of Materials, Politehnica University Timişoara, Timisoara, Romania
E-mail: dan.serban@upt.ro

H. Filipescu
Department of Mechatronics, Politehnica University Timişoara, Timisoara, Romania

Published online: 09 September 2020

ε^{t}	Engineering tensile strain
$\bar{\varepsilon}_{\mathrm{D}}^{\mathrm{pl}}$	Critical plastic strain
$\bar{\varepsilon}^{\mathrm{pl}}$	Equivalent plastic strain
$\dot{\bar{\varepsilon}}^{\mathrm{pl}}$	Equivalent plastic strain rate
η	Stress triaxiality
$\bar{\theta}$	Lode angle
ν	Poisson's ratio
ξ	Lode angle parameter
$\boldsymbol{\sigma}$	Stress tensor
$\bar{\boldsymbol{\sigma}}$	Effective stress tensor
σ^{c}	Engineering compressive stress
σ^{t}	Engineering tensile stress
σ_{ij}	Stress tensor components
σ_i	Principal stresses
$\boldsymbol{\sigma}'$	Deviatoric stress tensor
σ'_{ij}	Deviatoric stress tensor components
σ_{y}	Equivalent yield stress
Φ	Yield function
ψ	Dissipated plastic energy
ω	Damage initiation parameter

1 Introduction

Polyurethane rigid (PUR) foams represent a class of lightweight materials that, due to their mechanical and thermal properties, are used in a wide range of applications such civil engineering (thermal insulating panels), naval industry (composite panels with good floatability), railway transportation, automotive and aerospace applications (composite panels with good mechanical properties at low specific weights) [1–3].

Previous work performed by the authors was concerned with the experimental determination of the flexural properties of sandwich beams composed of 1050 H24 aluminium alloy faces and PUR cores of two densities (100 kg/m^3 and 300 kg/m^3), bonded together using Araldite AW 106 resin/Hardener HV 953U epoxy adhesive [4]. Two types of beams were tested, one with compact cores and the other with a perforated pattern [4].

The aim of this study is to develop constitutive models for the sandwich beam components that can accurately replicate the mechanical response as well as the occurring damage. Emphasis was placed on the calibration of constitutive models for the polyurethane foam, as the complex state of stress that occurs during the flexural loading of the perforated core has a decisive role on the failure of the beams.

Due to the brittle failure of PUR foams, previous studies were concerned with the application of various linear elastic fracture mechanics concepts (such as the Generalized Maximum Tangential Stress model, the Theory of Critical Distances, or the Averaged Strain Energy Density theory) in evaluating the structural integrity [5–7]. In this work, an elastic–plastic approach was considered, the failure of the material being modelled with the assumption that the critical plastic strain is a function of the stress triaxiality and of the Lode angle parameter.

2 Plasticity and damage

The mechanical behaviour of materials is assumed to be dependent on three invariants:

- the first invariant of the stress tensor I_1

$$I_1 = \mathrm{tr}\,(\boldsymbol{\sigma}) = \sum_{i=1}^{3} \sigma_{ii} \tag{1}$$

- The second invariant of the deviatoric stress tensor J_2

$$J_2 = \frac{1}{2} \sum_{i,j=1}^{3} \left(\sigma'_{ii} \sigma'_{jj} - \sigma'_{ij} \sigma'_{ji} \right) \tag{2}$$

- The third invariant of the deviatoric stress tensor J_3

$$J_3 = \det\left(\sigma'\right) = \sum_{i,j,k=1}^{3} \sigma_{ij}^{'}\sigma_{jk}^{'}\sigma_{ki}^{'} \tag{3}$$

In order to better understand the influence of these invariants, physical interpretations are often used in defining various material models.

The hydrostatic pressure (mean stress) p is defined as a function of the first invariant of the stress tensor. The sign of p denotes whether the body or element is subjected to tensile loadings ($p > 0$) or compressive loadings ($p < 0$). Expressed as a function of the principal stresses, it is defined as [8]:

$$p = \frac{I_1}{3} = \frac{\sigma_1 + \sigma_2 + \sigma_3}{3}[\text{MPa}] \tag{4}$$

The von Mises equivalent stress q is defined as a function of the second invariant of the deviatoric stress, and it is linked to the distortional energy consumed during deformation:

$$q = \sqrt{3J_2} = \frac{1}{\sqrt{2}}\left[(\sigma_1 - \sigma_2)^2 + (\sigma_2 - \sigma_3)^2 + (\sigma_3 - \sigma_1)^2\right]^{\frac{1}{2}}[\text{MPa}] \tag{5}$$

Considering the aforementioned stress measures, the stress triaxiality η is defined as:

$$\eta = \frac{p}{q}[-] \tag{6}$$

The third invariant can be normalized to a corresponding stress value r, defined as:

$$r = \left[\frac{27}{2}J_3\right]^{\frac{1}{3}} = \left[\frac{1}{2}(2\sigma_1 - \sigma_2 - \sigma_3)(2\sigma_2 - \sigma_1 - \sigma_3)(2\sigma_3 - \sigma_1 - \sigma_2)\right]^{\frac{1}{3}}[\text{MPa}] \tag{7}$$

The influence of the third invariant is expressed through the Lode angle parameter ξ:

$$\xi = \left[\frac{r}{q}\right]^3 = \frac{3}{2}\sqrt{3}\frac{J_3}{J_2^{\frac{3}{2}}} \in [-1, 1] \tag{8}$$

The Lode angle parameter characterizes the loading type a body/element is subjected to. Its extreme values denote uniaxial compression and equibiaxial tension ($\xi = -1$), uniaxial tension and equibiaxial compression ($\xi = 1$), while for shear $\xi = 0$.

The most commonly used yield criterion was formulated by Richard von Mises, and it is expressed as a function of the second invariant of the stress deviator J_2:

$$\Phi = J_2^2 - \frac{\sigma_y^2}{3} \tag{9}$$

Though accurate for steels, other classes of materials (such as aluminium alloys) exhibit different yielding behaviours when the Lode angle parameter does not equal -1 or 1. In consequence, several third invariant-dependent yield criteria were proposed, such as Hosford's criterion, Eq. (10a) [9], or the Bai–Wierzbicki criterion, Eq. (10b) [10].

$$\Phi = (\sigma_1 - \sigma_2)^{2k} + (\sigma_2 - \sigma_3)^{2k} + (\sigma_3 - \sigma_1)^{2k} - 2\sigma_y^{2k} \tag{10a}$$

$$\Phi = q - \sigma_y\left[1 - c_\eta\left(\eta - \frac{1}{3}\right)\right]\left[c_\theta^s + \left(c_\theta^{ax} - c_\theta^s\right)\left(\gamma - \frac{\gamma^{m+1}}{m+1}\right)\right] \tag{10b}$$

where γ is a parameter dependent on the Lode angle $\bar{\theta}$

$$\gamma = \frac{\sqrt{3}}{2 - \sqrt{3}}\left[\sec\left(\frac{\bar{\theta}\pi}{6}\right) - 1\right] \tag{10c}$$

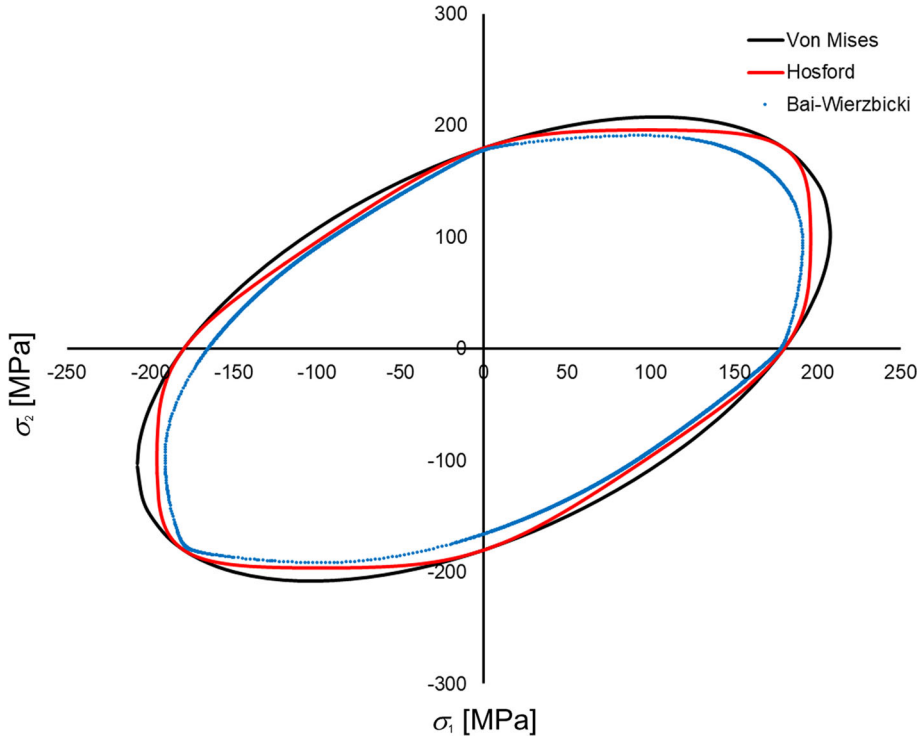

Fig. 1 von Mises, Hosford and Bai–Wierzbicki yield surfaces for plane stress conditions

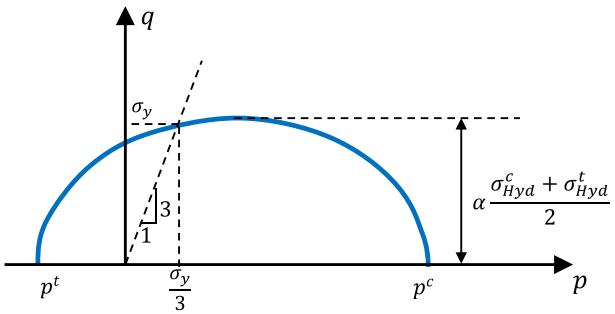

Fig. 2 Deshpande–Fleck yield surface in the p–q plane

$$\bar{\theta} \quad = \quad 1 - \frac{2}{\pi}\arccos\left(\xi\right) \tag{10d}$$

and $c_\eta \quad c_\theta^s$, c_θ^{ax}, c_θ^s and m are material parameters that are calibrated from experimental data (Fig. 1).

Constitutive models for crushable cellular materials take into account the effects of the hydrostatic pressure on yielding. The most commonly used model was proposed by Deshpande and Fleck [11] and defines the yield function as:

$$\Phi = \sqrt{q^2 + \alpha^2\left[p^{\mathrm{c}} - p^{\mathrm{t}}\right]^2} - \alpha\frac{p^{\mathrm{c}} + p^{\mathrm{t}}}{2} \tag{11}$$

where p^{c} and p^{t} are the yield stress in hydrostatic compression and tension, respectively, and α is a parameter dependent on the hydrostatic yield stress and on the uniaxial yield stress in compression. The shape of the initial yield surface in the p–q plane is presented in Fig. 2.

The damage formulation assumed in this work is based on the principle of nucleation and subsequent growth of voids in the material during loading [12]. This process modelled in two steps: the initiation of damage when a certain criterion is met (void nucleation) and the evolution of damage, which consists of the progressive reduction in element stiffness (void growth) [13,14].

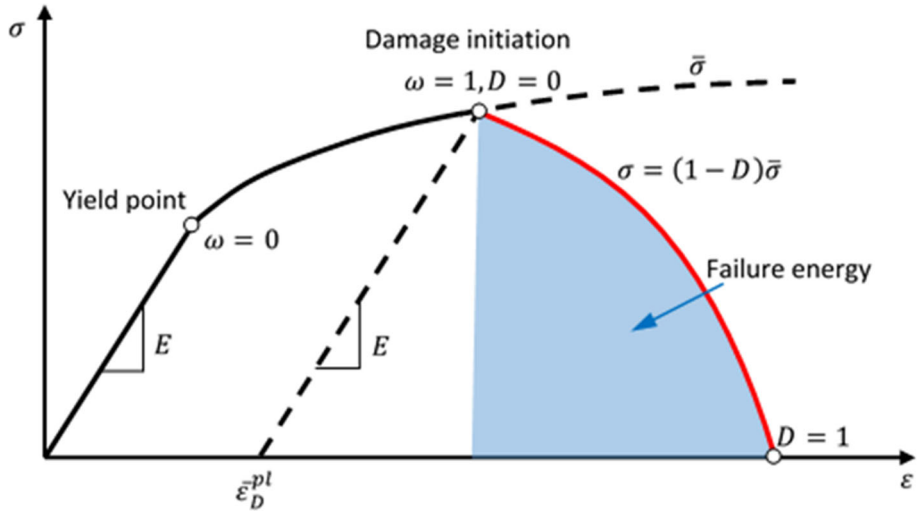

Fig. 3 Stress–strain evolution at an integration point for the ductile damage model

The chosen model for the damage initiation criterion assumes that the degradation of the material occurs when a certain equivalent critical plastic strain $\bar{\varepsilon}_{\mathrm{D}}^{\mathrm{pl}}$ is reached, which is a function of the stress triaxiality, the Lode angle parameter ξ and the equivalent plastic strain rate $\dot{\bar{\varepsilon}}^{\mathrm{pl}}$

$$\bar{\varepsilon}_{\mathrm{D}}^{\mathrm{pl}} = f\left(\eta, \xi, \dot{\bar{\varepsilon}}^{\mathrm{pl}}\right) \tag{12}$$

Therefore, the damage initiation parameter ω is expressed as:

$$\omega = \int \frac{d\bar{\varepsilon}^{\mathrm{pl}}}{\bar{\varepsilon}_{\mathrm{D}}^{\mathrm{pl}}} \tag{13}$$

where $\bar{\varepsilon}^{\mathrm{pl}}$ is the equivalent plastic strain:

$$\bar{\varepsilon}^{\mathrm{pl}} = \int \dot{\bar{\varepsilon}}^{\mathrm{pl}} \mathrm{d}t = \int \left(\sqrt{\frac{2}{3}\dot{\varepsilon}_{ij}^{\mathrm{pl}}\dot{\varepsilon}_{ij}^{\mathrm{pl}}}\right) \mathrm{d}t \tag{14}$$

When $\omega = 1$, the damage initiation conditions are met and the stress at an integration point will be calculated with the relation:

$$\boldsymbol{\sigma} = (1 - D)\,\bar{\boldsymbol{\sigma}} \tag{15}$$

where $\boldsymbol{\sigma}$ is the stress tensor, $\bar{\boldsymbol{\sigma}}$ is the effective (undamaged) stress tensor and D is the damage evolution parameter. The damage evolution parameter D progressively reduces the effective stress in an integration point, and if reaches a value of 1 (when a given criterion is reached, such as dissipated energy ψ or plastic displacement d), the element is excluded from the analysis. The damage evolution can be defined as a linear function, an exponential function or can be input as tabular data [13]

In summary, this degradation model assumes that when a critical plastic strain is reached (and subsequently $\omega = 1$), the effective stress from an integration point is gradually reduced through a damage evolution law ($D = f(\psi)$ or $D = f(d)$) until $D = 1$ and $\boldsymbol{\sigma} = 0$, at which point the element is considered to have failed and is removed (Fig. 3).

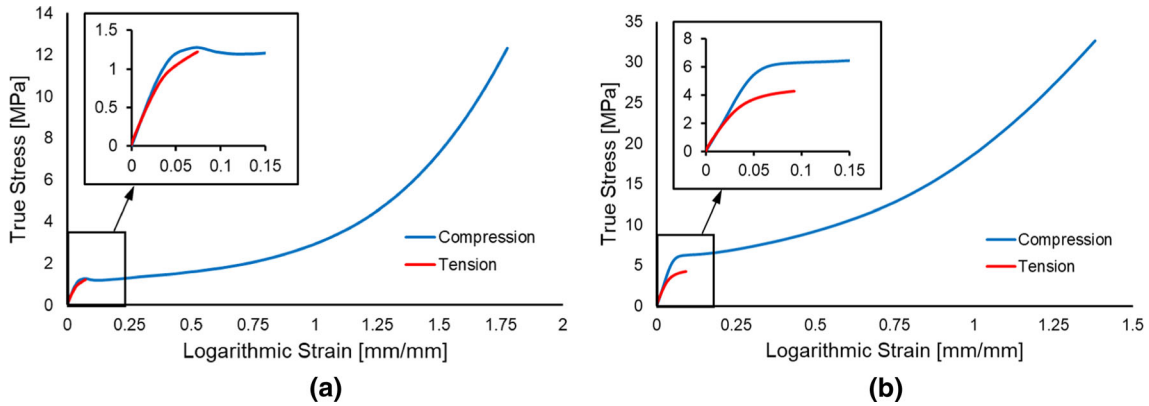

Fig. 4 Tensile and compressive results for 100 kg/m^3 (**a**) and 300 kg/m^3 (b)

3 Preliminary tests and material model calibration

3.1 Polyurethane rigid foams

The mechanical properties of the polyurethane foams were investigated for compression, tension and bending. Compression tests were performed on 25 mm sided cubes, while tensile tests were performed on ISO 527 dog-bone specimens [15]. The recorded (engineering) stress–strain values were converted to true stress–logarithmic strain values with the equations:

$$e^{\mathrm{c}} = -\ln\left(1 - \left|\varepsilon^{\mathrm{c}}\right|\right) \tag{16a}$$

$$e^{\mathrm{t}} = \ln\left(1 + \varepsilon^{\mathrm{t}}\right) \tag{16b}$$

$$s^{\mathrm{c}} = \frac{\left|\sigma^{\mathrm{c}}\right|}{\left(1 + \nu\left|\varepsilon^{\mathrm{c}}\right|\right)^2} \tag{16c}$$

$$s^{\mathrm{t}} = \frac{\sigma^{\mathrm{t}}}{\left(1 - \nu\varepsilon^{\mathrm{t}}\right)^2} \tag{16d}$$

The true stress–logarithmic strain curves in absolute values for tension and compression are presented in Fig. 4 for both investigated densities. Tensile tests show an elastic–plastic response characteristic for a semi-brittle material (low plastic strains at failure) while the compression tests exhibit the three stages of deformation characteristic to cellular materials [16].

It can be observed that the tensile and compressive stiffness is similar in the case of both densities, but the tensile yield points are lower, the difference being more pronounced for the 300 kg/m^3 density.

Considering the fact that the tensile behaviour of the materials determines the failure, the material models were calibrated after the tensile stress–strain curves. Having no volumetric data, the material parameters required to calibrate the Deshpande–Fleck model were chosen as $p^{\mathrm{c}} = p^{\mathrm{t}} = \sigma_{\mathrm{y}}$ and $\alpha = 0$, thus resulting a von Mises yield function. The hardening functions extracted from the true stress–logarithmic strain curves [17,18] and implemented in Abaqus yield accurate results (Fig. 5).

3.2 Tests on aluminium sheets and AW106 adhesive

The mechanical properties of the aluminium and adhesive were evaluated in tensile loadings on dogbone specimens [15,19] at room temperature, with a crosshead travel of 1 mm/min, the strains being recorded with an extensometer. The material models consisted of linear elasticity with von Mises plasticity and isotropic hardening, the plasticity data being extracted from the true stress–logarithmic strain values as described above. A damage model was calibrated for each material, considering the recorded failure plastic strain at a stress triaxiality value of 0.33 (corresponding to the uniaxial tensile loading). For the adhesive, the values were input as tabular data, while for the aluminium, the Johnson–Cook damage model (Eq. (17), [20]) was calibrated,

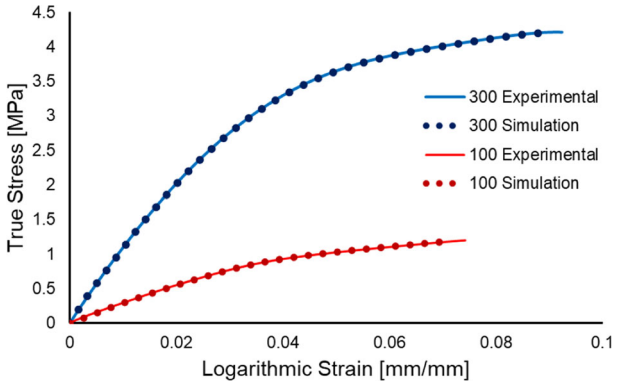

Fig. 5 Experimental and numerical results for tensile tests

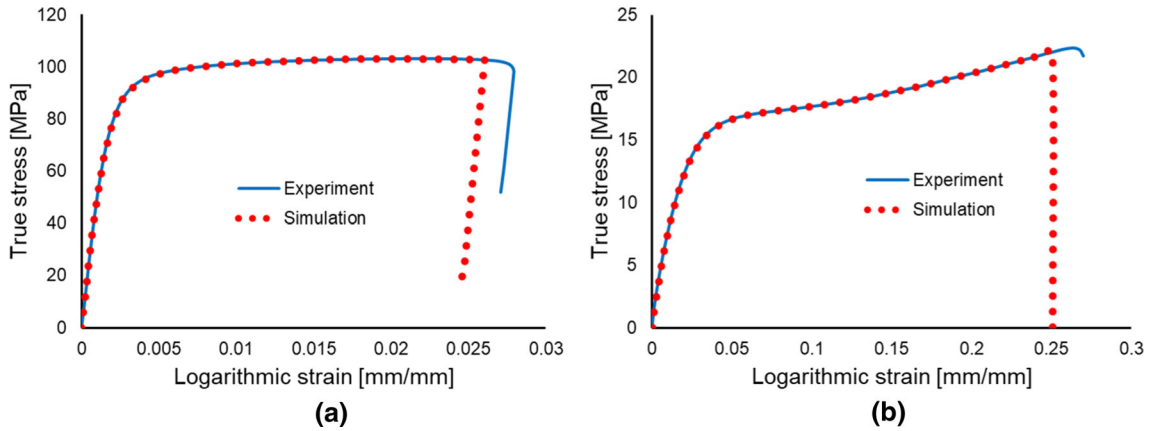

Fig. 6 Experimental an numerical results for aluminium sheets (a) and adhesive (b)

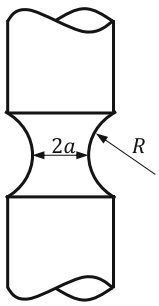

Fig. 7 Notched round bar specimen

with the parameters $d_1 = 0.0104$, $d_2 = 0.097$ and $d_3 = 5.358$.

$$\bar{\varepsilon}_{\mathrm{D}}^{\mathrm{pl}}(\eta) = d_1 + d_2^{-d_3\eta} \tag{17}$$

Numerical analyses were performed in order to evaluate the material models, yielding good results (Fig. 6).

4 Determination of failure strain–stress triaxiality data on notched round specimens

The use of notched round bar specimens (Fig. 7) for the determination of the failure strain as a function of the stress triaxiality has been extensively used for metals [21–23].

The relation between the $a/2R$ ratio and stress triaxiality was evaluated according to Bridgman's analytical formula [23] and through numerical analyses (the values presented in Fig. 8 corresponding to the

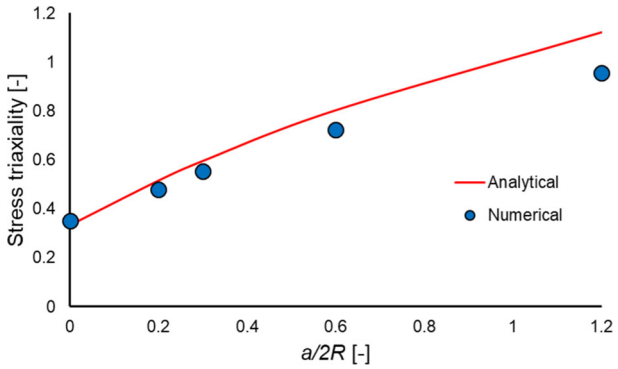

Fig. 8 Analytical and numerical results for the a/2R influence on the stress triaxiality

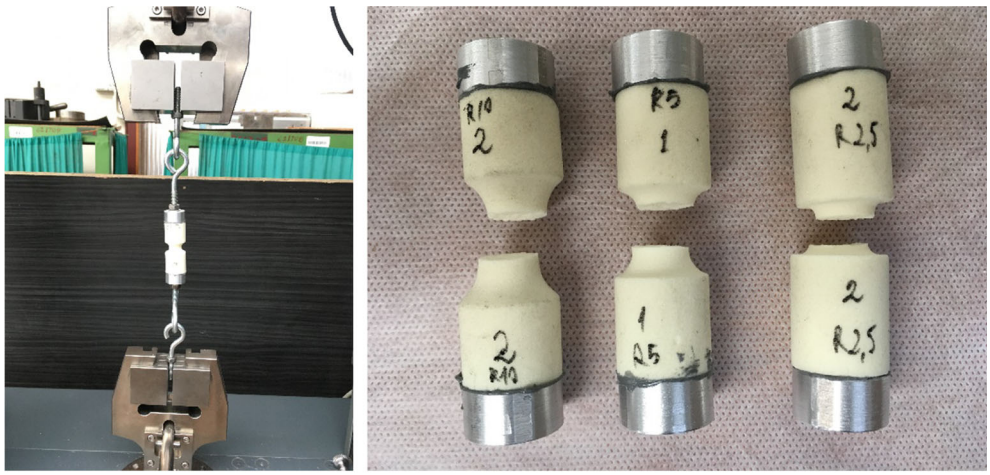

Fig. 9 Notched cylindrical specimen setup (**a**) and fractured samples (**b**)

onset of plasticity). For the experimental procedures, five $a/2R$ ratios were chosen: 0 (plane stress tension); 0.2; 0.3; 0.6; 1.2.

$$\eta = \frac{1}{3} + \ln\left(1 + \frac{a}{2R}\right) \tag{18}$$

The specimens used in this study were machined (through turning) from cylinders with a diameter of 20 mm, the notches being obtained using profiled tools. The diameter of the critical region was $2a = 12$ mm for all specimens, the profiled tools having radii R of 2, 5 mm, 5 mm, 10 mm and 15 mm, respectively. The overall height of the specimens was around 60 mm.

In order to avoid the effect of direct clamping, the specimens were fixed to aluminium cylindrical tabs (using the AW106 adhesive) and the gripping was perform with the help of steel hooks that were threaded into the tabs in order to align the specimens with the machine axis (Fig. 9a).

The tests were performed at 1 mm/min crosshead travel speed with preload of $5N$. Three specimens were tested for each configuration, and the graphs depicting representative stress–displacement curves for each geometry are presented in Fig. 10.

Figure 10 shows that the third invariant of the stress deviator (and consequently the Lode angle parameter) has an influence on the plasticity of the polyurethane foams (with a more pronounced effect on the 300 kg/m^3 density), as lower values for the radii (and higher stress concentration) determine an earlier yielding point. In consequence, the Von Mises yield surface might not determine accurate simulation results.

In order to determine the critical plastic strain and stress triaxiality values, each specimen was measured before testing and CAD models were generated respecting the dimensions. For the mesh, second-order tetrahedral elements were used (C3D10M), with mesh refinement in the notch region (the number of element varying from 0.8×10^6 to 1.7×10^6 as shown in Fig. 11), using the material models described in Paragraph 3.1.

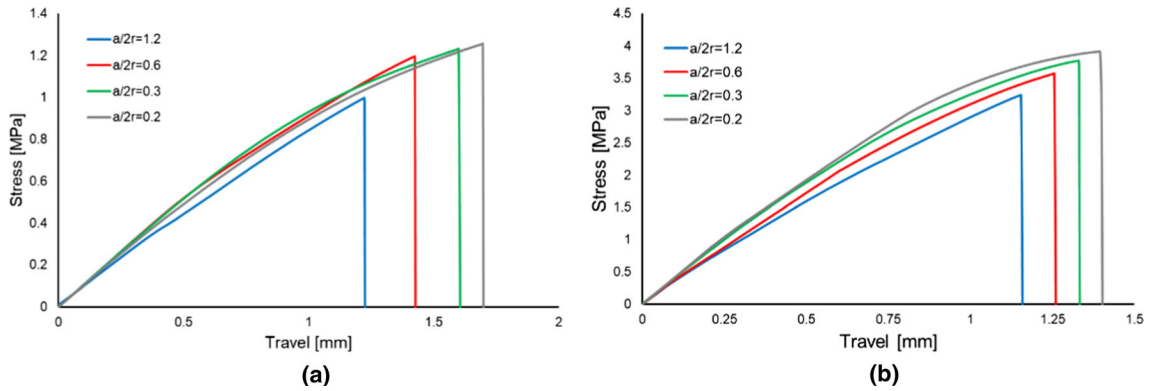

Fig. 10 Experimental results for the notched round specimen tests for 100 kg/m^3 (**a**) and 300 kg/m^3 (**b**)

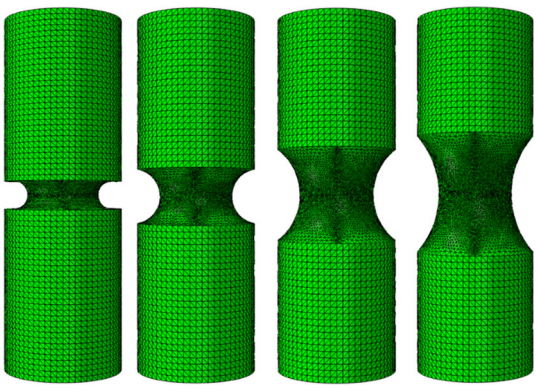

Fig. 11 Meshed models used in numerical analyses

The clamping system was considered rigid, and thus, the recorded displacement at failure was attributed to the top surface of the specimen (the bottom surface being fixed). When the given displacement is reached, node paths were defined across the critical region, recording the variation in equivalent plastic strain, stress triaxiality, von Mises equivalent stress and the third invariant with the radius. The results are plotted in Fig. 13 for both densities with the origin of the coordinate system corresponding to the centre of the specimen.

From Fig. 12, it can be observed that neither parameter is constant throughout the cross sections of the specimens at failure. Considering the extreme values, Fig. 13 presents the variation in the critical plastic strain with the stress triaxiality for the contour (assuming that the failure was initiated at the surface of the specimen) and for the middle of the cross section (assuming that the failure was initiated in the centre of the specimen). It can be observed that, at a given stress triaxiality, the model assuming that the failure occurs in the centre of the specimens fails much earlier. For instance, using the critical plastic strain–stress triaxiality curve obtained from the centre of the specimen would determine a shorter travel at failure for the specimens with $a/2R = 1.2$: at a stress triaxiality of 0.5, the critical plastic strain at the surface of the specimens would be 0.024 mm/mm, as opposed to the 0.077 mm/mm, as obtained by the imposed displacement at failure. This may be due to the influence of the Lode angle parameter, as it is reaches a value of $\xi = 0.43$ at the surface of the specimen while in the centre it remains constant at $\xi = 1$ for the failure of all geometries. Therefore, it can be hypothesized that the failure initiates at the surface of the specimen, where the Lode angle parameter is smaller, and, for larger values (maximal value of 1 in the case of the centre of the specimen), the critical plastic strain would be higher than the one recorded during the analyses.

5 Validation of the failure model on composite beams

The composite sandwich beam models consisted of five components: two 1.5-mm-thick aluminium faces, two 0.5-mm-thick adhesive layers and a 28-mm-thick PUR core. Two core geometries were considered, one

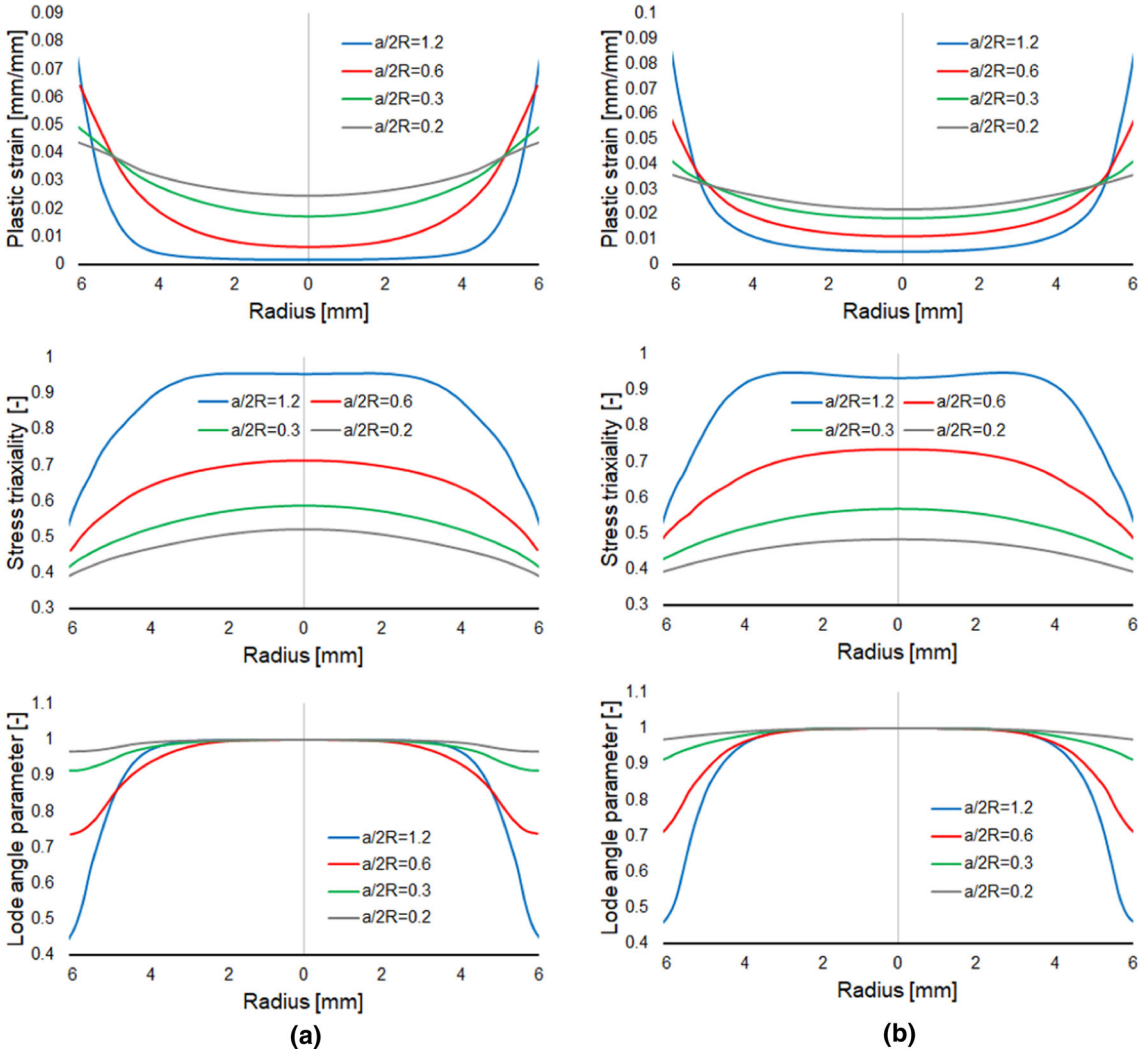

Fig. 12 Plastic strain, stress triaxiality and Lode angle parameter variation with radius for 100 kg/m^3 (**a**) and 300 kg/m^3 (**b**)

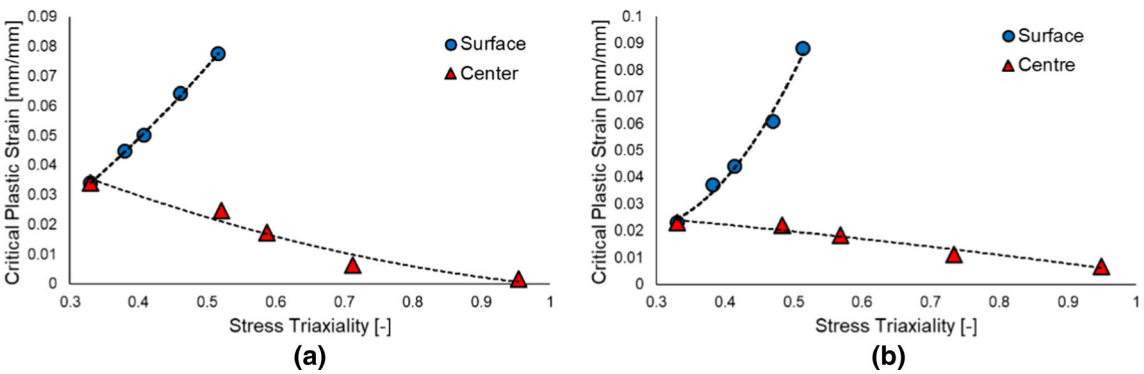

Fig. 13 Critical plastic strain variation with stress triaxiality in the centre on the specimen and at the surface for 100 kg/m^3 (**a**) and 300 kg/m^3 (**b**)

compact and one with a perforated pattern, with holes of ϕ7.5 mm and ϕ18 mm (Fig. 14a). The length of the beams was 400 mm and the width 70 mm.

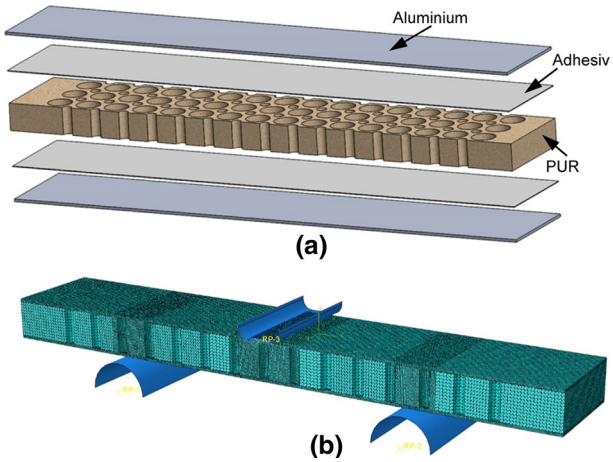

Fig. 14 Exploded view of the composite sandwich beam components, presenting the geometry of the perforated core (**a**) and the meshed model (**b**)

Table 1 Damage input data

	Equivalent plastic strain	Stress triaxiality	Lode angle parameter		Equivalent plastic strain	Stress triaxiality	Lode angle parameter
100 kg/m^3	0.0341	0.33	1	300 kg/m^3	0.023	0.33	1
	0.0447	0.371	0.968		0.0372	0.382	0.964
	0.0501	0.408	0.915		0.044	0.414	0.904
	0.0641	0.461	0.736		0.0609	0.471	0.699
	0.0775	0.516	0.434		0.0881	0.514	0.451

The numerical analyses were performed in Abaqus using the *Explicit* solver. The quasi-static analyses were conducted using mass scaling, in order to reduce the computational time. All components were meshed with C3D10M elements (second-order tetrahedral elements with modified formulation), the size varying between 0.5 mm and 2 mm (a number of 10^6 elements, Fig. 14b).

The supports consisted of 20 mm radius rigid cylinders and the indentor was a filleted 30 mm wide rigid prism. The interaction properties consisted of normal behaviour with the "hard contact" formulation and tangential behaviour with a penalty formulation and a friction coefficient of 0.3.

The material models used in the analyses were described above, the damage data input for the PUR foams being presented in Table 1.

The damage input data represent spatial curves (the equivalent plastic strain at failure as a function of the stress triaxiality and the Lode angle parameter). The software determines the critical plastic strain for other η and ξ values through linear interpolations [13]. For the damage evolution law, a linear formulation was used with a failure energy of $0.01J$, as all the specimens exhibited sudden failure (Fig. 10).

The force–displacement curves for the experimental data and numerical analyses are presented in Fig. 15 for the compact core and in Fig. 16 for the perforated core (Fig. 17).

The beams having compact cores with densities of 100 kg/m^3 exhibited core indentation, while the beams with 300 kg/m^3 compact core failed through face yielding and subsequent core fracture (Fig. 16). Both these phenomena were replicated in the numerical analyses. The resulting force–deflection results are in good accordance with the experimental data, with some discrepancies in modelling the post-yielding behaviour of the 100 kg/m^3 specimens.

The beams with perforated cores failed through core shear, images of the failed beams with perforated cores compared to the numerical results being presented in Fig. 18, showing a good agreement in terms of crack propagation. In both scenarios, the initial failure occurred at the foam–adhesive interface (due to the stress concentration caused by different materials properties) with the crack propagating along the interface. Midway between the support and the indentor, the crack shifted its path along a 45° angle, until it reached the opposing interface. Regardless of the fact that the numerical model did not capture the crack split that occurred

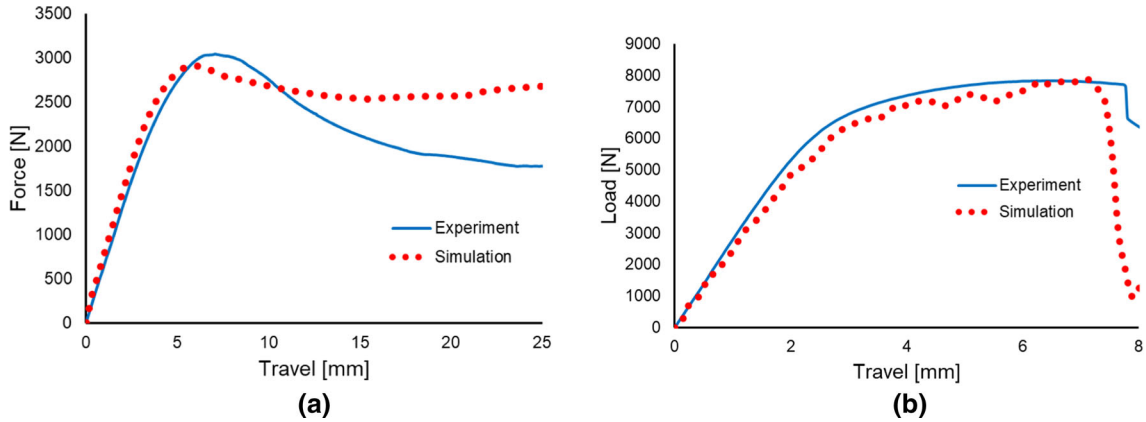

Fig. 15 Experimental and numerical results for flexural tests on composite beams with compact cores for 100 kg/m^3 cores (**a**) and 300 kg/m^3 cores (**b**)

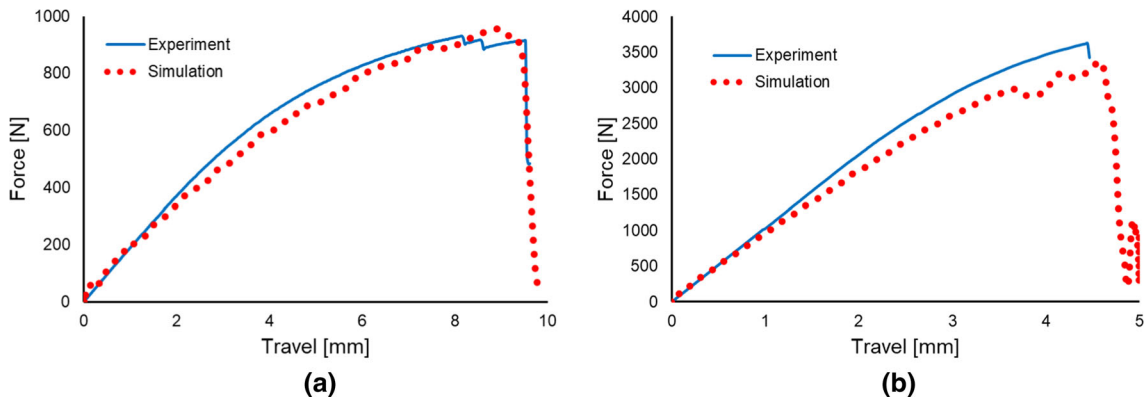

Fig. 16 Experimental and numerical results for flexural tests on composite beams with perforated cores for 100 kg/m^3 cores (**a**) and 300 kg/m^3 cores (**b**)

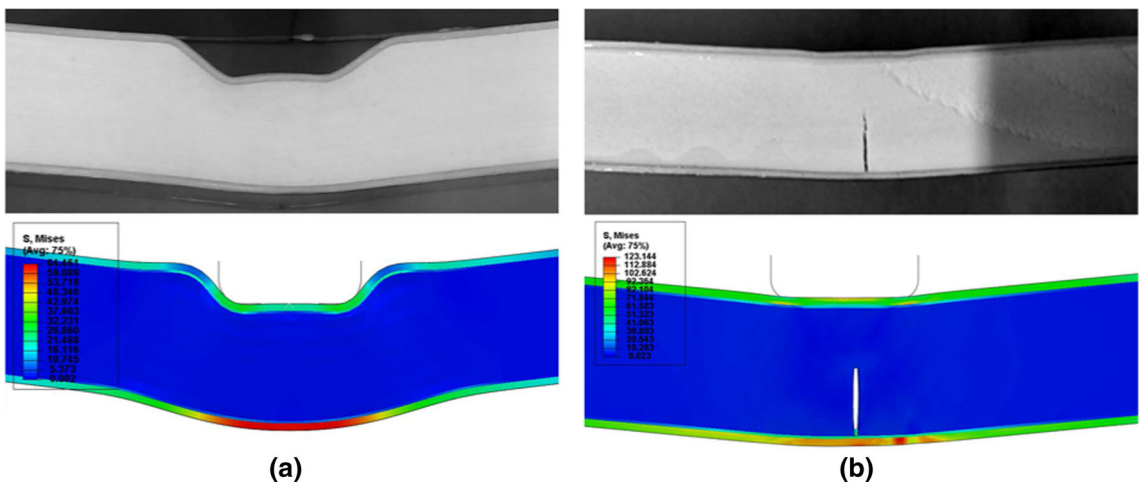

Fig. 17 Fractured specimen and simulation results for tests on composite beams with compact cores for 100 kg/m^3 (**a**) and 300 kg/m^3 (**b**)

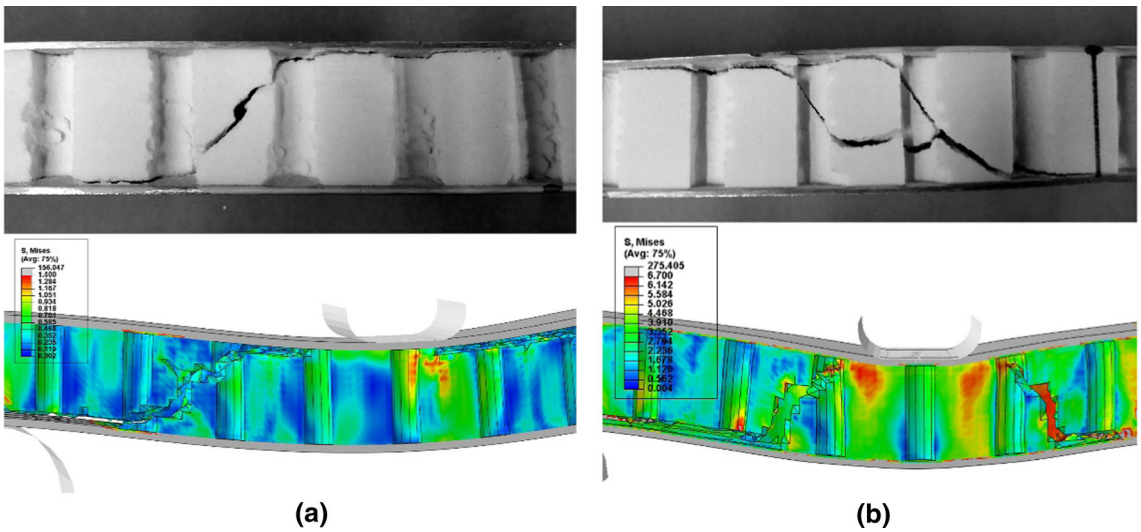

Fig. 18 Fractured specimen and simulation results for tests on composite beams with perforated cores for 100 kg/m^3 (**a**) and 300 kg/m^3 (**b**)

in the pictured 300 kg/m^3 specimen, the force–travel curves were in good agreement and the predicted failure deflections were accurate.

6 Discussions and conclusions

In this work, a damage model for semi-brittle materials was proposed, which assumes that the critical plastic strain is a function of the triaxial state of stress. The model was calibrated for positive stress triaxiality values, obtained through tests on cylindrical notched specimens with various radii, and was evaluated for flexural loadings of composite beams with aluminium faces and PUR cores.

Previous studies on the failure of rigid polyurethane foams assumed a linear elastic response, and the failure was evaluated with the help of fracture mechanics. Even though the investigated theories are able to predict the failure of PUR foams, their application to structures with complex geometries is cumbersome. This work assumes a different approach, which considers that failure occurs in the plastic domain, the critical strain being influenced by the triaxial state of stress, the third invariant of the stress deviator and the strain rate. This macroscopic failure model has the advantage of a facile numerical implementation, being suitable for the analysis of any type of structure and loading.

Though initially developed for metals and subsequently applied to polymers, the ductile damage model was shown in this study that is able to predict in a relatively accurate manner the damage and failure of the investigated semi-brittle materials subjected to complex stress states. The principle of void nucleation and growth can be considered valid for this class of materials, as this damage mechanism can be attributed to the fracture of the struts, which will determine void-like defects when a given number of cell walls fail.

Furthermore, this study shows that the triaxial state of stress is having a significant role in determining the failure of semi-brittle materials as more simplistic models; for example, ones based on principal stresses and strains at failure (used in XFEM analyses for instance) are unable to model the failure loci at different stress states. Consequently, this approach could be applied to other areas, such as fracture mechanics and fatigue. However, other continuum mechanics concepts, such as third invariant-dependent yield surfaces, should be applied in order to obtain an accurate response for this class of materials.

Numerical data obtained from the analyses on notched cylindrical specimens showed that the Lode angel parameter is crucial in understanding the failure in PUR foams. Thus, a complete failure model should include the influence of the Lode angle parameter, and further testing is required in order to obtain the failure surface ($\bar{\varepsilon}_{\mathrm{D}}^{\mathrm{pl}} = f(\eta, \xi)$) for the investigate PUR foams [10]. The influence of the strain rate was not considered, as only quasi-static tests were performed.

For the simulations performed on the notched cylindrical specimens, the use of 3D elements was chosen in detriment of a simplified 2D axisymmetric elements because of the increased number of integration points,

which determine a more accurate stress and strain distribution. In addition, identical C3D10M elements are used in the three-point bending analyses, assuring consistency between the material model evaluation and validation. The drawback of this approach is that the element size must be small in order to obtain convergence, which leads to long simulation times.

The simulation results for three-point bending showed a good agreement with the experimental values, even with the limited amount of data used to calibrate the failure model, concluding that this approach can be successfully applied in the design stage for components that are manufactured from PUR foams. Future work will focus on the determination of the failure loci for other stress triaxiality and Lode angle parameter values (obtained from biaxial, shear or Arcan tests) in order to obtain a complete failure surface.

Acknowledgements This work was supported by the Romanian National Authority for Scientific Research and Innovation, CCCDI—UEFISCDI, projects number PD 13/2018 and CCCDI—UEFISCDI, project number PN-III-P1-1.2-PCCDI-2017-0391/CIA_CLIM.

References

1. Gibson, L., Ashby, M.: Cellular Solids: Structure and Properties. Cambridge University Press, Cambridge (1997)
2. Şerban, D., Linul, E., Voiconi, T., Marsavina, L., Modler, N.: Numerical evaluation of two-dimensional micromechanical structures of anisotropic cellular materials: case study for polyurethane rigid foams. Iran. Polym. J. **24**, 515–529 (2015)
3. Şerban, D., Voiconi, T., Linul, E., Marşavina, L., Modler, N.: Viscoelastic properties of PUR foams: impact excitation and dynamic mechanical analysis. Materiale Plastice **52**, 537–541 (2015)
4. Marşavina, L., Şerban, D., Pop, C., Negru, R.: Experimental investigation of failure modes for sandwich beams. In: 16th International Conference on Fracture and Damage Mechanics. Key Engineering Materials, vol. 754, pp. 115–118 (2017)
5. Negru, R., Marşavina, L., Filipescu, H.: Evaluation of generalized MTS criterion for mixed-mode fracture of polyurethane materials. In: Advances in Fracture and Damage Mechanics XII, Key Engineering Materials, vol. 557–558, pp. 117–120 (2014)
6. Negru, R., Marşavina, L., Voiconi, T., Linul, E., Filipescu, H., Belgiu, G.: Application of TCD for brittle fracture of notched PUR materials. Theor. Appl. Fract. Mech. **80**, 87–95 (2015)
7. Marşavina, L., Berto, F., Negru, R., şerban, D., Linul, E.: An engineering approach to predict mixed mode fracture of PUR foams based on ASED and micromechanical modelling. Theor. Appl. Fract. Mech. **91**, 148–154 (2017)
8. Zapara, M.A., Tutyshkin, N.D., Müller, W.H., Weinberg, K., Wille, R.: A physico-mechanical approach to modeling of metal forming processes—part I: theoretical framework. Contin. Mech. Thermodyn. **20**, 231–254 (2008)
9. Hosford, W.: A generalized isotropic yield criterion. J. Appl. Mech. **39**(2), 607–609 (1972)
10. Bai, Y., Wierzbicki, T.: A new model of metal plasticity and fracture with pressure and Lode dependence. Int. J. Plast. **24**, 1071–1096 (2008)
11. Deshpande, V., Fleck, N.: Multi-axial yield behaviour of polymer foams. Acta Materialia **49**, 1859–1866 (2001)
12. Tutyshkin, N.D., Lofink, P., Müller, W.H., Wille, R., Stahn, O.: Constitutive equations of a tensorial model for strain-induced damage of metals based on three invariants. Contin. Mech. Thermodyn. **29**, 251–269 (2017)
13. Abaqus, "User's Manual," vol. Analysis (2017)
14. Şerban, D., Marşavina, L., Modler, N.: Finite element modelling of the progressive damage and failure of thermoplastic polymers in puncture impact. In: Proceedings of the XXIII Italian Group of Fracture Meeting, Procedia Engineering, vol. 109, pp. 97–104 (2015)
15. ISO 527, Plastics—Determination of Tensile Properties, International Standard Organization (1996)
16. Bleistein, T., Jung, A., Diebels, S.: A microsphere-based material model for open cell metal foams. Contin. Mech. Thermodyn. **32**, 255–267 (2020)
17. Şerban, D., Weber, G., Marşavina, L., Silberschmidt, V., Hufenbach, W.: Tensile properties of semi-crystalline thermoplastic polymers: effects of temperature and strain rates. Polym. Test. **32**, 413–425 (2013)
18. Şerban, D., Marşavina, L., Rusu, L., Negru, R.: Numerical study of the behavior of magnesium alloy AM50 in tensile and torsional loadings. Arch. Appl. Mech. **89**(5), 911–917 (2019)
19. ISO 6892-1, Metallic materials—tensile testing—part 1: method of test at room temperature. International Standard Organization (2019)
20. Murugesan, M., Jung, D.W.: Johnson Cook material and failure model parameters estimation of AISI-1045 medium carbon steel for metal forming applications. Materials **12**, 609 (2009)
21. Bao, Y., Wierzbicki, T.: On the cut-off value of negative triaxiality for fracture. Eng. Fract. Mech. **72**, 1049–1069 (2005)
22. Pineau, A., Benzerga, A., Pardeon, T.: Failure of metals I: Brittle and ductile fracture. Acta Materialia **107**, 424–483 (2016)
23. Bridgman, P.: Studies in Large Plastic Flow and Fracture—with Special Emphasis on the Effects of Hydrostatic Pressure. McGraw-Hill, New York (1952)